






## Article

# Parallelizable Microfluidic Platform to Model and Assess In Vitro Cellular Barriers: Technology and Application to Study the Interaction of 3D Tumor Spheroids with Cellular Barriers

Arya Lekshmi Nair <sup>1,2,†</sup>, Lena Mesch <sup>3,†</sup>, Ingo Schulz <sup>4</sup>, Holger Becker <sup>4</sup>, Julia Raible <sup>1</sup>, Heiko Kiessling <sup>1</sup>, Simon Werner <sup>1</sup>, Ulrich Rothbauer <sup>1,5</sup>, Christian Schmees <sup>1</sup>, Marius Busche <sup>1</sup>, Sebastian Trennheuser <sup>6</sup>, Gert Fricker <sup>6</sup> and Martin Stelzle <sup>1,\*</sup>

- <sup>1</sup> NMI Natural and Medical Sciences Institute, University of Tübingen, Markwiesenstraße 55, 72770 Reutlingen, Germany; arya.lekshmi1604@gmail.com (A.L.N.); jschuetz.tue@googlegmail.com (J.R.); heiko.kiessling@live.de (H.K.); Simon.werner@nmi.de (S.W.); Ulrich.Rothbauer@nmi.de (U.R.); Christian.Schmees@nmi.de (C.S.); mariusbusche@hotmail.de (M.B.)
- <sup>2</sup> Currently with Mimetas, De Limes 7, 2342 DH Oegstgeest, The Netherlands
- <sup>3</sup> Institut für Neuroanatomie und Entwicklungsbiologie, University of Tübingen, Österbergstraße 3, 72074 Tübingen, Germany; lena.mesch@uni-tuebingen.de
- <sup>4</sup> Microfluidic ChipShop GmbH, Stockholmer Str. 20, D-07747 Jena, Germany; Ingo.Schulz@microfluidic-chipshop.com (I.S.); hb@microfluidic-chipshop.com (H.B.)
- <sup>5</sup> Institute of Pharmacy and Molecular Biotechnology, University of Heidelberg, Im Neuenheimer Feld 364, 69120 Heidelberg, Germany; s.trennheuser@uni-heidelberg.de (S.T.); gert.fricker@uni-hd.de (G.F.)
- <sup>6</sup> Institute of Pharmacy, Pharmaceutical Biotechnology, Auf der Morgenstelle 8, D-72076 Tübingen, Germany
- \* Correspondence: martin.stelzle@nmi.de
- † These authors contributed equally to this work.



**Citation:** Nair, A.L.; Mesch, L.; Schulz, I.; Becker, H.; Raible, J.; Kiessling, H.; Werner, S.; Rothbauer, U.; Schmees, C.; Busche, M.; et al. Parallelizable Microfluidic Platform to Model and Assess In Vitro Cellular Barriers: Technology and Application to Study the Interaction of 3D Tumor Spheroids with Cellular Barriers. *Biosensors* **2021**, *11*, 314. <https://doi.org/10.3390/bios11090314>

Received: 28 July 2021

Accepted: 31 August 2021

Published: 3 September 2021

**Publisher's Note:** MDPI stays neutral with regard to jurisdictional claims in published maps and institutional affiliations.

**Abstract:** Endothelial and epithelial cellular barriers play a vital role in the selective transport of solutes and other molecules. The properties and function of these barriers are often affected in case of inflammation and disease. Modelling cellular barriers in vitro can greatly facilitate studies of inflammation, disease mechanisms and progression, and in addition, can be exploited for drug screening and discovery. Here, we report on a parallelizable microfluidic platform in a multiwell plate format with ten independent cell culture chambers to support the modelling of cellular barriers co-cultured with 3D tumor spheroids. The microfluidic platform was fabricated by microinjection molding. Electrodes integrated into the chip in combination with a FT-impedance measurement system enabled transepithelial/transendothelial electrical resistance (TEER) measurements to rapidly assess real-time barrier tightness. The fluidic layout supports the tubeless and parallelized operation of up to ten distinct cultures under continuous unidirectional flow/perfusion. The capabilities of the system were demonstrated with a co-culture of 3D tumor spheroids and cellular barriers showing the growth and interaction of HT29 spheroids with a cellular barrier of MDCK cells.

**Keywords:** cellular barriers; microfluidic device; TEER; tumor spheroids; Fourier-transform impedance spectroscopy



**Copyright:** © 2021 by the authors. Licensee MDPI, Basel, Switzerland. This article is an open access article distributed under the terms and conditions of the Creative Commons Attribution (CC BY) license (<https://creativecommons.org/licenses/by/4.0/>).

## 1. Introduction

Cells lining the vasculature form barriers separating blood from its surrounding tissues and play a vital role in the selective transport of solutes and other molecules across these barriers. Endothelial cells that constitute the lumen of intact blood vessels form a continuous monolayer that acts as a barrier between blood and the surrounding tissues [1,2]. Epithelial cells serve as a protective layer lining the inside and outside cavities of the human body. Both epithelial and endothelial cells are interconnected via specialized tight junctions or zona occludens that render selective permeability to these barriers [2]. Barrier integrity is crucial for physiological function and homeostasis. Barrier tightness varies between organs and also between different vascular segments of the same organ [1].

For instance, endothelial cells that make up the highly specialized blood–brain barrier (BBB) of the central nerve system (CNS) possess unique barrier properties and differ in their permeability compared to any other endothelial barrier of the body [3].

In many cases of chronic inflammation and disease, the integrity of the cellular barriers protecting vital organs of the human body tends to be disturbed. For instance, persistent neuroinflammation that has been reported in the pathology of almost all neurodegenerative disorders is accompanied by a disruption in the BBB integrity [4,5]. In addition, physical remodeling and disruption of endothelial cell barriers with increased permeability were observed during transmigration of tumor cells in the context of intravasation and extravasation, which are key steps associated with cancer metastasis [6–9]. Furthermore, hyperpermeability and loss of integrity of intestinal barriers were noted in the pathogenesis of several gastrointestinal disorders such as inflammatory bowel disease [10,11]. These examples highlight the importance of modelling cellular barriers to advance our understanding of barrier integrity. Significant progress has been made in clarifying the underlying mechanisms of endothelial and epithelial barrier function in both physiological and pathological contexts [12–14]. However, our understanding of barrier integrity and their disruption in events of trauma, injury or inflammation is far from complete. Therefore, *in vitro* models that better recapitulate the physiology, variability and complexity of cellular barriers are under rapid development and may be exploited to study inflammation, disease mechanisms and progression [15–24]. These models possess enormous potential in advancing drug development and discovery by developing techniques and approaches that could facilitate the delivery of therapeutic drug candidates across these barriers [25,26] to reach their target tissue and successfully treat diseases of organs protected by these barriers.

To enable efficient drug screening and toxicity studies, *in vitro* models of cellular barriers must exhibit the characteristics and properties seen *in vivo*, such as the expression of junctional proteins and complexes. Transwell-based platforms are most often used to model cellular barriers *in vitro*; however, they lack critical properties such as the shear forces associated with physiological blood flow [27,28]. As a result, some cell types can lack important markers or transporters that are found *in vivo*, thereby limiting the suitability of these platforms to reflect their physiological relevance *in vitro*. Furthermore, these models lack the 3D microenvironment, complex cell–cell and cell–matrix interactions observed *in vivo*. On the other hand, animal models closely resemble the level of structural and functional complexity seen in humans, but they only allow limited control and manipulation of experimental conditions, raise ethical concerns and are also expensive [29], time consuming, have limited availability and are poor predictors of human outcomes due to species–specific differences [30,31]. Thus, there is a pressing need for improved *in vitro* systems that better mimic the tissue complexity and physiology [32,33].

With the advent of microfluidic organ-on-chip technology, it has become easier to model miniaturized healthy and diseased human tissues *in vitro* with increased physiological relevance. Advancement in microfabrication, microfluidics, biomaterials and tissue engineering techniques have been exploited to establish relevant test systems via the co-culture of multiple cell types, with cells often embedded in a hydrogel, to recapitulate the 3D spatial organization, complexity and heterogeneity of *in vivo* tissues [34–36]. A number of research groups have been successful in developing models of cellular barriers with important insights into cell culture conditions, morphology, viability and integrity of barriers in a microfluidic chip, and their potential in drug screening applications, particularly in the context of modelling the blood–brain barrier [18,20,21,23,37,38]. Also, devices to model aspects of cancer physiology and development have been presented [39,40]. However, most of these devices were fabricated from PDMS. While PDMS presents advantages such as ease of fabrication, biocompatibility and gas permeability, PDMS-based chips tend to adsorb substances [41,42], which is a major concern for drug screening applications, given that most of the drugs are hydrophobic in nature. In most cases, chip fabrication is based on soft lithography, which does not allow for seamless upscaling of device numbers. Yet, validation procedures and the demonstration of robustness and reproducibility in

real world applications will clearly require the availability of a large number of devices. In addition, perfusion is often achieved by pressure-driven flow through tubing using syringe pumps. While tube-connected systems yield well-controllable flow rates, they are difficult to parallelize and are not easily adaptable to conventional cell culture and drug development workflows.

Therefore, we exploited microfluidic technology to model cellular barriers in a parallelizable microfluidic platform manufactured by microinjection molding of cyclic olefin copolymer (COC) comprising integrated electrodes to enable real-time transepithelial/transendothelial electrical resistance (TEER) measurement.

Continuous unidirectional flow was achieved by means of gravitation-driven flow in combination with an incubator compatible perfusion system. TEER was measured by employing a custom-made parallelized fast Fourier transform (FFT)-impedance spectrometer. As an example, and to demonstrate the versatility of this device, we established the complete workflow ranging from cell seeding to the generation of co-cultures of tumor cells growing in a hydrogel mimicking tumor extracellular matrix (ECM) along with a cellular barrier. Here, we show preliminary data to demonstrate how this system can be used to monitor the growth of micro-tumors and their interaction with a cellular barrier and migration into the perfusion channel.

## 2. Materials and Methods

### 2.1. Device Microfabrication

The microfluidic chip (MFC) was manufactured from cyclic olefin copolymer (COC) by microfluidic ChipShop GmbH, Jena, Germany. COC is transparent and exhibits low autofluorescence. It comprises ten micro channels with five different layouts of pillar size and gap width (Figures 1 and A1, Table A1). The mold inserts used for injection molding were fabricated in-house at microfluidic ChipShop by ultraprecision micro-milling.

The chip body was manufactured by precision injection molding. The channel depth was 170  $\mu\text{m}$ . The process yields devices with excellent optical properties and low substance adsorption [43]; the latter may be further reduced by functional coatings if necessary [44,45]. Shadow masks were made by laser machining in thin steel foils and used to deposit electrodes by vacuum evaporation of titanium (10 nm) acting as adhesion promoter and gold (100 nm). Shadow masks were aligned carefully with respect to the open microfluidic structures to generate electrodes on the side walls next to the cultivation areas and connecting leads (golden-colored structures in Figure 1) and were kept in place by means of permanent magnets located underneath the chip fixture.

Finally, microfluidic structures, electrodes and connecting leads were covered by bonding a thin (approx. 140  $\mu\text{m}$ ) COC foil onto the bottom of the chip, leaving connecting pads open to enable electric connection to the electrodes.

The described fabrication process is scalable in regard to numbers and yields devices in reproducible quality.

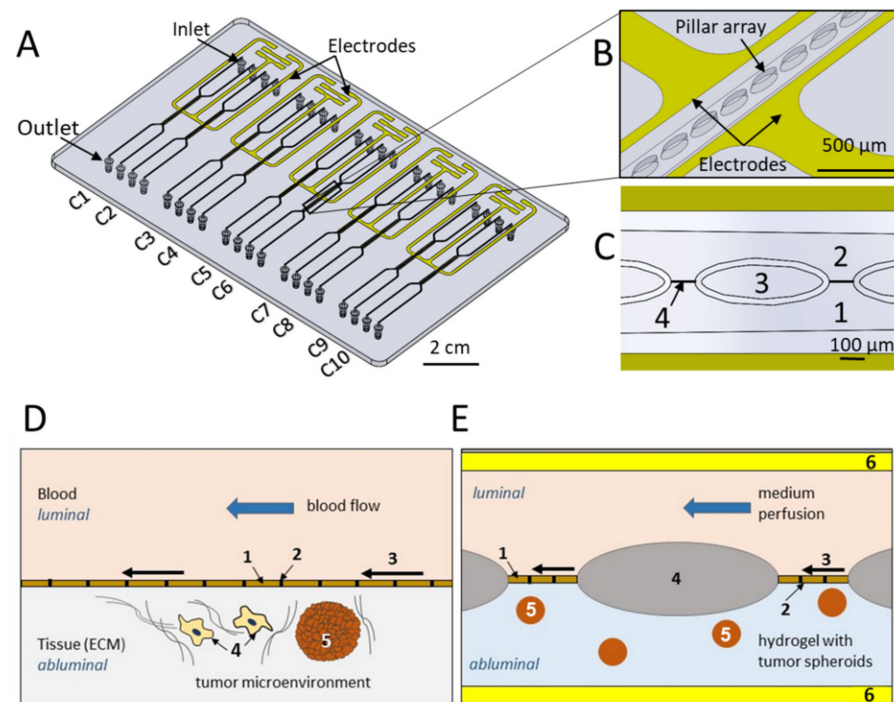


**Figure 1.** Chip technology: (A) precision injection molded device with multi-well-plate footprint, comprising 10 culture areas C1 to C10 with two channels, inlets and outlets per culture area. (B) Electrodes line the culture area with contact pads positioned at the plate edge (A). (C) Within the culture areas, both channels are separated by an array of pillars. Aqueous, low viscous hydrogel solution with or without cells may be introduced in one of the channels (“abluminal channel”) whereby gaps between pillars act as capillary stop valves preventing spilling of the gel solution into the adjacent channel (“perfusion channel” or “luminal channel”). (D) Scheme of tumor–vascular interface showing endothelial barrier (1) with cells forming tight junctions (2). Blood flow results in shear forces (3). Immune cells (4) invade tissue to attack tumor tissue (5). (E) Scheme of chip according to this study mimicking the tumor–vascular micro-environment by co-culture of tumor spheroids (5) in a hydrogel matrix with a cellular barrier (1) grown on the interface formed between pillars (4). Electrodes (6) located at the periphery of both channels enable measurement of the electrical impedance across the interface.

## 2.2. Integration of Gel Matrix

Each culture area is divided into two channels by a micro pillar array (Figure 1B): the abluminal side, which corresponds to tissue, is initially filled with a hydrogel solution comprising HT29 cells, which then polymerizes and establishes a smooth gel surface between two adjacent pillars (Figure 1C–E). Pillar spacing was designed in such a way (Figure A1) that adjacent pillars act as capillary stop valves that prevent the spillover of hydrogel solution into the luminal channel during priming. The luminal side, which represents the blood capillary, was filled with cell culture medium and was later seeded with cells, which form a cellular barrier on the gel interface, thus sealing the space between the pillars. Thus, the micro pillar array within each channel offered spatial control over the hydrogel that resembles the extracellular matrix in the chip. The reagents for the hydrogel were obtained from Cellendes GmbH, Reutlingen, Germany and mixed as indicated by the manufacturer ([www.cellendes.com](http://www.cellendes.com)) before filling the microfluidic chip. The pre-gel solution mixture was filled into the abluminal side of the micro channels with the help of a syringe pump under a constant flow rate of 2.5 µL/min (Video S1). The incubation period for complete gelation of the hydrogel was ca. 90 min.

Perfusion in the microfluidic chip during cell culture was achieved by force of gravity, employing a parallelized perfusion setup (Figure 2). To this end, the inlet and the outlet



ports of each channel were fitted with reservoirs ( $V \approx 1$  mL). Different volumes of cell culture medium were placed into the reservoirs such that a level difference and the associated pressure difference induce flow through the channel. A parallelized peristaltic micro-pump equipped with flexible tubes reaching into both outlet and inlet reservoirs returns the perfused medium from the outlet reservoir to the inlet reservoir, thus maintaining the level difference. Pumping rate, duration of the pumping period, and duration of the waiting period as well as the level of tubing within the reservoirs can be adjusted separately as required for a particular experimental situation. Flow rate depends on the level difference between the inlet and outlet reservoir and may be adjusted between approximately 10 and 100  $\mu\text{L}/\text{min}$ . Reservoirs for the perfusion set-up were made by cutting 1–5 mL pipette tips to a length of ca. 37 mm. The end of the tip was cut and slightly shortened in such a way as to fit tightly onto the inlet and outlet ports of the chip. Flexible silicone tubes (ID. 1.0  $\times$  OD. 2.0 mm) to be used with two 6-channel micro-peristaltic pumps (Takasago Fluidic) were prepared at a length of ca. 13–15 cm. The reservoirs and tubes were autoclaved prior to use. Silicone plugs were made using the SYLGARD 184 Silicone Elastomer Kit (Dow Corning Inc., Miland, MI, USA) and used to tightly cover the gel-filled channels of the MFC to prevent evaporation. The medium flowing through the perfusion channel has no contact with these plugs.

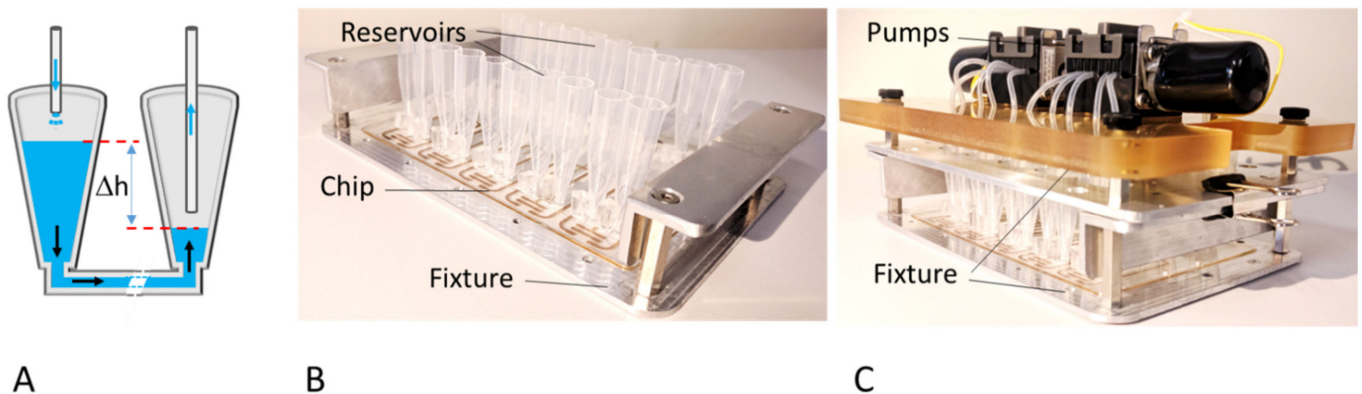


**Figure 2.** Parallelized perfusion setup: (A) Scheme of gravitation-driven flow. Medium reservoirs ( $V \approx 1$  mL) were placed on the channel inlet and outlet. Tubes reaching into the reservoirs in connection with micro-peristaltic pumps that operated intermittently were used to move perfused medium from the outlet reservoir back to the inlet reservoir, thus maintaining the level difference,  $\Delta h$ , driving unidirectional medium flow. (B) Chip in fixture with medium reservoirs attached on fluid ports of MFC. (C) Perfusion setup with 10 channel microfluidic pumps mounted on top of the chip fixture to yield an easy-to-use and incubator compatible perfusion system.

### 2.3. TEER Measurement Setup

TEER measurements employed a custom-made parallelized FFT impedance spectroscopy system used to measure impedance across cellular barriers between 1 Hz and 10 kHz (Figure 3). For the measurement, the device was taken out of the incubator and placed on the connector board. The system generates and simultaneously applies a discrete spectrum of sinusoidal signals to all culture areas on the chip in a parallel fashion. Both the voltage and current signal were recorded at high temporal resolution. Following data acquisition, Fourier transforms of both the voltage and current signals were computed and rendered the impedance spectra, which allowed for the determination of several electrical parameters of the system by using a non-linear fitting algorithm to 2-parameter (no cellular barrier present) or a 4-parameter equivalent circuit model (cellular barrier present) (Figure A2). Following the measurements, the device was remounted into the perfusion setup and placed in the incubator for further cultivation under continuous perfusion.

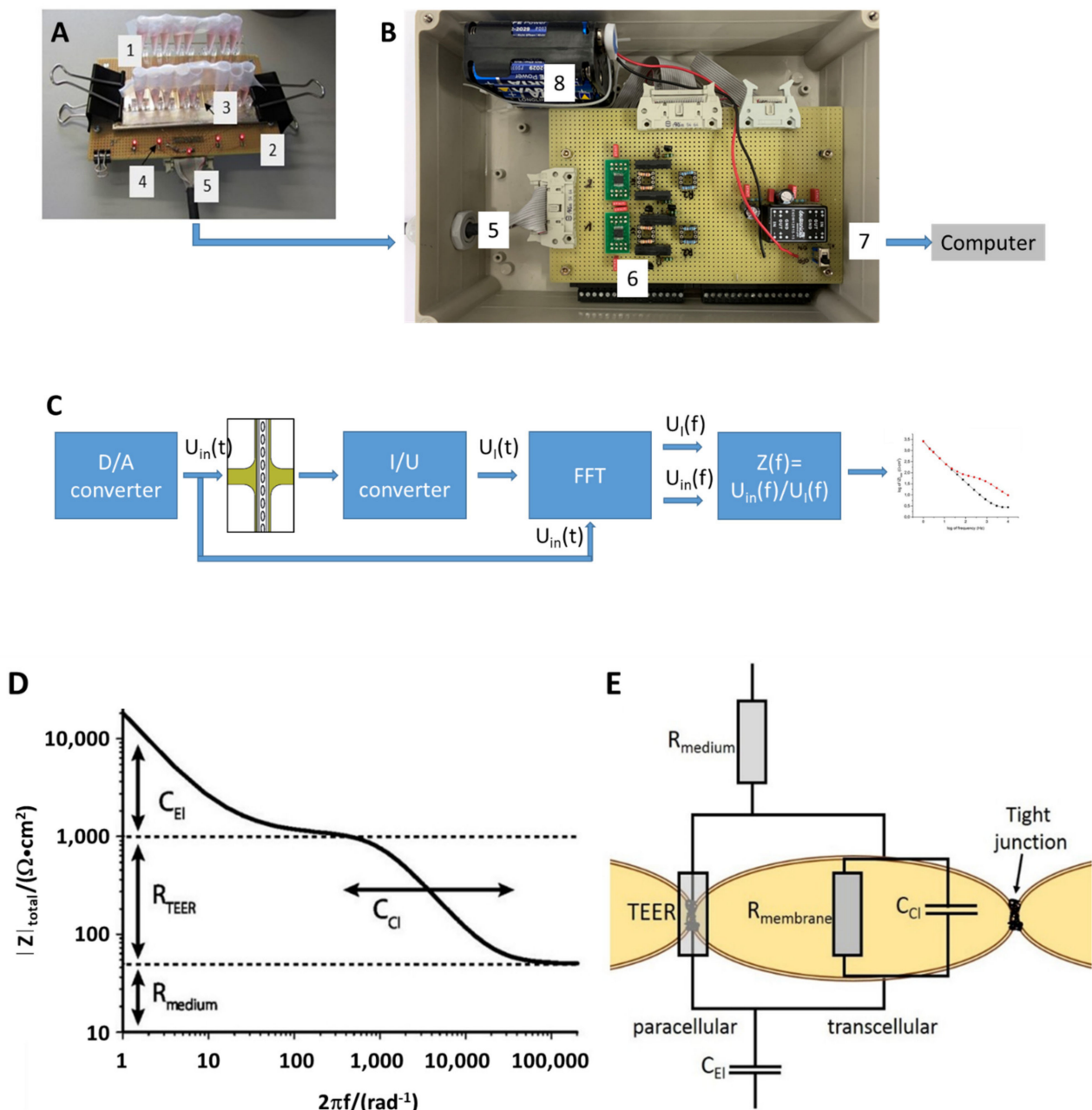


**Figure 3.** TEER measurement setup: (A) Chip (1) with medium-filled reservoirs (3) mounted on electrical interface fixture (2). LEDs (4) indicate proper connection of chip contacts to the measurement system. A cable (5) delivers the voltage signal,  $U_{in}(t)$ , to the 10 culture areas simultaneously and feeds individual current signals,  $U_i(t)$ , to the current-to-voltage converter (6) in the measurement system. (B) Measurement system comprising a power supply (8), a digital/analog converter (D/A), current-to-voltage converters (I/U), digital switches, and data acquisition board (National Instruments USB9012) connected to a computer via USB-cable (7). (C) Schematic circuit diagram: the D/A-converter provides a voltage signal synthesized from a set of discrete frequencies to the chip. Voltage amplitudes may be adjusted by the LabView application software. Fourier transform of both current and voltage signals yields frequency spectra thereof and allows for calculation of the impedance spectra  $Z(f)$  of 10 channels within seconds. (D) Impedance spectra measured in the MFC exhibit distinct features reflecting the electrical properties (adapted from [46] with permission) (E) of electrodes,  $C_{EI}$ , medium,  $R_{medium}$ , and interface with or without cellular barrier, TEER,  $R_{membrane}$  and  $C_{dI}$ .

#### 2.4. Hydrogel Preparation

The reagents were obtained from Cellendes GmbH, Reutlingen, and mixed as indicated by the manufacturer ([www.cellendes.com](http://www.cellendes.com)) before the microfluidic chip was filled as shown in Table 1.

**Table 1.** Reagent volumes for 120  $\mu\text{L}$  gel for one MFC.

3-D Life Reagents	V ( $\mu\text{L}$ )	V ( $\mu\text{L}$ )
10 $\times$ CB (80% pH 7.2, 20% pH 5.5)	2.4	9.6
Water	15.3	61.2
SG-PVA (30 mmol/L SH-reactive groups)	2.5	10.0
RGD Peptide (20 mmol/L SH groups)	0.8	3.2
Cell suspension (HT29)	6.0	24.0
CD-Link (20 mmol/L SH groups)	3.0	12.0
Total	30.0	120.0

Cellendes 3-D Life Hydrogel is a two-component system consisting of a thiol-reactive polyvinyl alcohol (PVA) polymer and a thiol-functionalized crosslinker (CD-Link) which comprises a matrix-metalloproteinase cleavable peptide allowing embedded cells to cleave the crosslinker and migrate within the gel. Mixing the two components leads to the formation of stable thioether bonds and formation of the gel. Gelation time varies with pH and can be adjusted by mixing two ten-fold concentrated buffers (10 $\times$  CBpH 7.2 and 10 $\times$  CBpH 5.5). The lower the pH, the slower the gel formation. Peptides containing cell adhesion motifs such as RGD can be covalently attached to a fraction of the thiol-reactive groups of the thiol-reactive polymer, either prior to or after crosslinking to support adhesion of cells. Since crosslinking with CD-Link causes the pre-gel solution mixture to start to solidify in less than 3 min at room temperature, it was added to the reagent mixture just before the gel filling process was started. The prepared gel complex was placed on ice and the MFC was placed on a cold surface for gel filling to maximize the gelation time as much as possible.

#### 2.5. Preparation and Seeding of Cells into Chip

HT29 Human colon adenocarcinoma cells were cultured and maintained at 5%  $\text{CO}_2$  at 37  $^\circ\text{C}$  in T75 cell culture flasks, and passaged by dissociation with 0.05% trypsin/EDTA every two to three days at a confluency of 70–90%. Cell suspension for the experiments was prepared by centrifugation of dissociated cells at 130 $\times$  g for 7 min at RT.

A cell strainer with a pore size of 40  $\mu\text{m}$  was employed to extract single HT29 cells in suspension, which is crucial to generate similarly sized tumor spheroids in the MFC. Each 30  $\mu\text{L}$  volume of hydrogel composition comprised 6  $\mu\text{L}$  cell suspension at a density of  $2 \times 10^6$  cells/mL. HT29 cells were seeded at  $\approx 1600$  cells per abluminal channel as each channel was filled with ca. 4  $\mu\text{L}$  gel.

A fresh microfluidic chip was UV sterilized for 30 min. The gel was infused into the channels using a previously sterilized syringe pump set-up as described above. After gel filling, the MFC was placed in an upright position under the sterile hood and incubated for ca. 60–90 min to allow for gelation.

MDCK cells stably expressing a Vimentin specific chromobody [47] (MDCK VB6-CB) were labeled with CellTracker<sup>TM</sup> Red (Invitrogen) prior to seeding and cultivation in the microchip to enable real-time visualization of the interaction of tumor spheroids (previously stained with Calcein-AM on-chip) with the MDCK cell barrier. The dye was dissolved in 20  $\mu\text{L}$  high-quality DMSO to prepare a stock solution at RT; 3  $\mu\text{L}$  of this stock solution was diluted in 500  $\mu\text{L}$  PBS to prepare the CellTracker<sup>TM</sup> Red working solution. The dye is well retained in living cells through several generations.

Each channel was filled with 10  $\mu\text{L}$  of MDCK cell suspension ( $10^7$  cells/mL, i.e.,  $10^5$  cells per channel). After cell seeding, the reservoirs were covered with Parafilm and the chip was placed in an upright position in the incubator for approximately 2 h to facilitate

the adhesion of cells to the gel surface. After incubation, fresh medium was added to the reservoirs and the perfusion setup was switched on. The medium was changed once every two days. The formation of a cellular barrier across the gel interface and the interaction with tumor spheroids was monitored regularly using a fluorescence microscope (Nikon Eclipse Ti).

### 3. Results

#### 3.1. Chip Fabrication

Generally, devices manufactured by precision injection molding show a certain degree of shrinkage after solidification of the polymer melt in the molding tool and the subsequent cooling after demolding. In an iterative process, shadow masks used for electrode deposition were modified to reflect the actual position of the culture areas as opposed to the nominal values provided in the CAD design. Shadow masks were kept in place by magnetic forces during electrode deposition by vacuum evaporation. A precision of  $<50\ \mu\text{m}$  was achieved for the electrode placement over the dimensions of the wellplate-sized chips. The bottom foil exhibits excellent optical properties and no autofluorescence was observed.

Priming of the MFC depended on pillar size and spacing as well as on the filling rate,  $V_F$ . A parameter  $\alpha$  was defined according to

$$\alpha = \text{width}_{\text{pillar}} \cdot \text{distance}_{\text{pillars}} \quad (1)$$

Success rate decreased linearly with increasing  $\alpha$  (Figure A3).

Perfusion rate depends on the level difference between the inlet and outlet reservoir. Flow rates ranging from 10 to 100  $\mu\text{L}/\text{min}$  were applied. The resulting shear stress was calculated by multi-physics simulation (Figure A5). At a 10  $\mu\text{L}/\text{min}$  flow rate, the shear stress ranges from 0.01 to 0.045 Pa, about an order of magnitude lower than what is estimated based on in vivo values [48,49].

#### 3.2. Cellular Barriers in MFC

MDCK cells stably expressing a green fluorescent Vimentin chromobody (MDCK\_VB6-CB) [47] adhered and formed a tight layer on both the functionalized gel interface as well as on the channel surface, i.e., chip material (Figure 4). The chip-integrated electrodes were used to determine the electrical properties of the cellular barrier by means of FFT impedance spectroscopy.

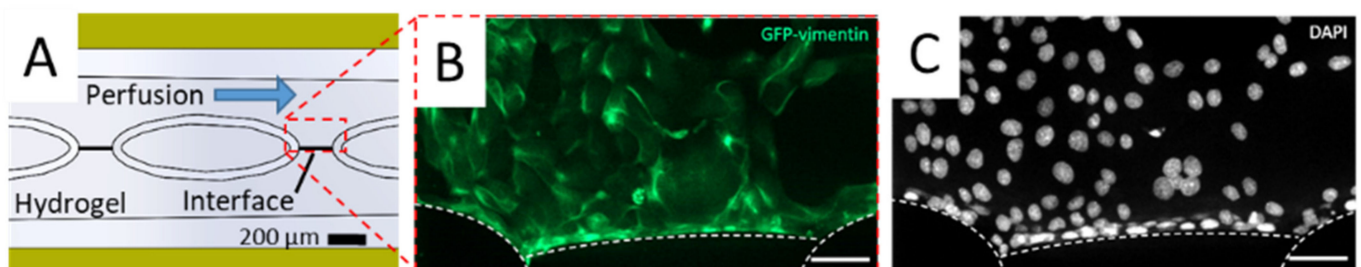


**Figure 4.** Fluorescence microscopy characterization of cellular barriers in MFC. (A) Schematic figure of location of cellular barrier on the interface between gel phase and perfusion channel. (B), (C) Cellular barrier comprised of MDCK\_VB6-CB cells. Cells are located on the interface between the perfusion channel and hydrogel as well as on the surface of micro pillars and proliferate to eventually cover the complete surface of the perfusion channel. Cells expressing green fluorescent Vimentin chromobody (VB6-CB B) were fixed with PFA and DAPI staining was performed (C). Cells were seeded at a density of  $10^5$  cells per channel at passage 3. Staining was performed at day five after seeding. Single slice confocal microscope image at bottom of the channel. Scale bar 50  $\mu\text{m}$ .

A clear correlation between TEER and the cell density of MDCK\_VB6-CB cells was observed. MDCK\_VB6-CB cells seeded and grown at higher densities yielded relatively dense layers, as demonstrated by TEER values of about 50–80  $\Omega \cdot \text{cm}^2$  (Figure 5B). Fitting of



the data to the 4-parameter equivalent circuit (Figure A2) also yields the capacitance of the gel–medium interface (in the absence of cells) and the cellular layer and enables calculation of coverage,  $\Theta$ , (Figure A2). In these preliminary experiments, a coverage of up to 100% was observed with MDCK\_VB6-CB cells.

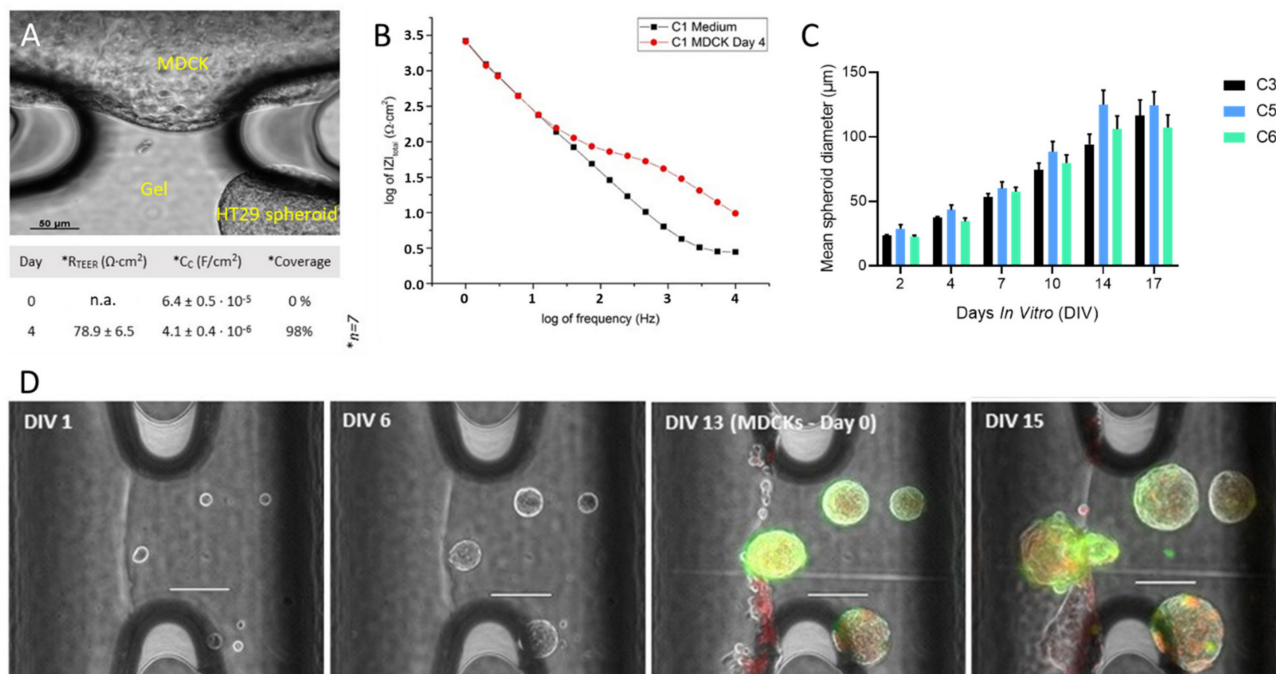


**Figure 5.** Co-culture of HT29 tumor spheroids with a cellular barrier of MDCK\_VB6-CB cells. (A) Typical micrograph of culture area no. 1 showing the perfusion channel and gel interface between pillars completely lined by MDCK\_VB6-CB cells and HT29 tumor spheroid growing in gel phase. An average TEER of 78.9 ± 6.5 Ωcm<sup>2</sup> at DIV4 was observed from  $n = 7$  culture areas. The interfacial capacitance,  $C_c$ , yielded an average coverage of 98%. (B) Typical impedance spectra of interface (culture area no. 1, corresponding to image in (A)) without a cellular barrier (black dots) at day 0 and at day 4 of MDCK\_VB6-CB cells (red dots), respectively. TEER: 58.7 Ωcm<sup>2</sup>; lines represent the least square fit to data using the equivalent circuit display in Figure A2A. (C) Growth of HT29 tumor spheroids in three different channels during a period of 17 days, with 2 days under static conditions, and thereafter under continuous perfusion. Mean diameter of spheroids increased from 25 μm to 120 μm. Error bars indicate standard deviation calculated from  $n = 8$  micro-spheroids. (D) Micrographs showing the growth of tumor spheroids in the gel phase under continuous perfusion, their interaction with a leaky cellular barrier of MDCK\_VB6-CB cells (also labelled with CellTracker™ Red) and finally the outgrowth of a tumor spheroid into the perfusion channel at day 15.

### 3.3. Tumor Spheroid Growth, Migration and Interaction with Cellular Barrier in MFC

The 3D growth of HT29 tumor cells seeded in PVA-hydrogel was studied (Figure 5C). Individualized cells were obtained by sieving the cell suspension. Cells were pelleted and mixed with the gel solution, which was then injected into the channels of the MFC. An initial growth period of 2 days without perfusion was required to observe the growth of 3D tumor spheroids. If the perfusion of medium was started immediately after the gel set, the cells would not grow in size although they remained viable as confirmed by Calcein-AM staining (not shown). The size of the spheroids increased linearly over a cultivation period of 14 days (Figure 5C) following the initial 2-day period under static conditions.

HT29 spheroids were co-cultured with a MDCK\_VB6-CB cellular barrier (Figure 5A,D). MDCK\_VB6-CB cells were seeded on DIV13. Spheroids remained viable as confirmed by Calcein-AM/propidium iodide staining. In case of a leaky cellular barrier, tumor spheroids were observed to remodel and leave the gel phase and grow towards the perfusion channel.

## 4. Discussion

### 4.1. Chip and Periphery Instrumentation, Workflow Compatibility

We have demonstrated a microfluidic device with integrated TEER electrodes and a complete process for establishing and analyzing co-cultures of cellular barriers with micro-tumors in a parallelized fashion.

Successful chip priming depends on the pillar width and spacing, as is to be expected as gaps between pillars act as capillary stop valves and a larger pillar-to-pillar distance will result in lower burst pressure [50].

The device fabrication relies on scalable precision injection molding technology of COC. Integrated TEER electrodes in combination with FFT-impedance spectroscopy enable rapid assessment of electrical properties of cellular barriers and coverage. However, the shrinkage of chips following demolding required iterative adaptation of shadow masks to the actual dimensions of the MFCs in order to achieve precise positioning of electrodes.

A chemically defined hydrogel was functionalized by an RGD-peptide and was shown to support prolonged growth and adhesion of MDCK cells. A cleavable peptide crosslinker (CD-link) enabled remodeling by 3D tumor spheroids and their outgrowth into the perfusion channel.

The incubator-compatible perfusion system enables gravitation-driven unidirectional flow vs. bidirectional flow as found in other models [51]. It integrates seamlessly into common cell culture workflows.

However, the need for certain improvements also became apparent: in a future design, fluid connectors could be implemented in a standard industry format and spacing on the chip. Silicone tubing used with peristaltic pumps may cause unwanted absorption of compounds [41,42] and it also contributes to the overall dead volume in the system, which should be minimized. Accordingly, there is a need for parallelized, low dead volume pumping schemes to support the application of parallelized organ-on-chip *in vitro* models. Finally, a third channel could be added to the cell culture areas to enable assessment of substance transfer and retrieval from the *in vitro* model for further analysis [52].

### 4.2. Cell Culture in MFC

The feasibility and versatility of cell culture in the MFC in general was demonstrated by cultivation of the cellular barriers of MDCK, and also in the co-culture with HT29 tumor spheroids in the adjacent gel phase.

TEER measured using the integrated electrodes generally was significantly lower than that seen in earlier reports [53–55]. We hypothesize that the interface between cellular layer and chip material may represent an ion leakage in cases where cells only adhere on the functionalized gel surface. In contrast to designs with a co-planar orientation of the cellular barrier [2,56,57] with the chip plane, in our design, the cellular barrier is composed of 22 individual patches with the outer rim contacting the chip material. The resistance is very sensitive towards even minor ion leaks [2,58] (Figure A3). On the other hand, capacitance provides a reliable measure of overall coverage (Figure A2).

The inhibition of cell growth in HT29 tumor spheroids under perfusion at the beginning of the culture may be due to the unintended dilution of factors secreted by the cells in case of an excess liquid to cell ratio and highlights the issue of finding and establishing the proper liquid to cell ratio (LoC) in microfluidic *in vitro* models [59]. As relatively high LoC values are often found in microfluidic *in vitro* models, this should receive more attention in future technical developments of organ-on-chip (OoC) models. However, proper manipulation of minute volumes of fluid while maintaining constant perfusion and avoiding effects such as pinning of meniscus to edges and evaporation certainly poses a significant technical challenge.

## 5. Conclusion

In summary, we demonstrated a parallelized microfluidic device and a comprehensive workflow to study and analyze co-cultures of cellular barriers and 3D tumor spheroids under continuous unidirectional flow.

**Supplementary Materials:** The following are available online at <https://www.mdpi.com/article/10.3390/bios11090314/s1>, Video S1: suppl.info.video\_1\_gel\_filling.

**Author Contributions:** Conceptualization, J.R., G.F. and M.S.; Data curation, A.L.N., L.M., H.K. and S.T.; Funding acquisition, J.R. and M.S.; Investigation, A.L.N., L.M., I.S., H.K. and S.T.; Methodology, I.S., H.B. and S.W.; Project administration, J.R., G.F. and M.S.; Supervision, G.F., J.R., and M.S.; Visualization, A.L.N., L.M., U.R., C.S. and M.B.; Writing—original draft, A.L.N., L.M. and M.S.; Writing—review & editing, L.M., M.B., S.T. and M.S. All authors have read and agreed to the published version of the manuscript.

**Funding:** This research was supported by the State Ministry of Baden-Wuerttemberg for Economic Affairs, Labour and Tourism and the Federal Ministry of Education and Research (BMBF) through grant 16SV5952.

**Informed Consent Statement:** Not applicable.

**Data Availability Statement:** Not applicable.

**Acknowledgments:** Helpful discussions with E. Haltner and P. Wagner are acknowledged.

**Conflicts of Interest:** The authors declare no conflict of interest.

## Appendix A

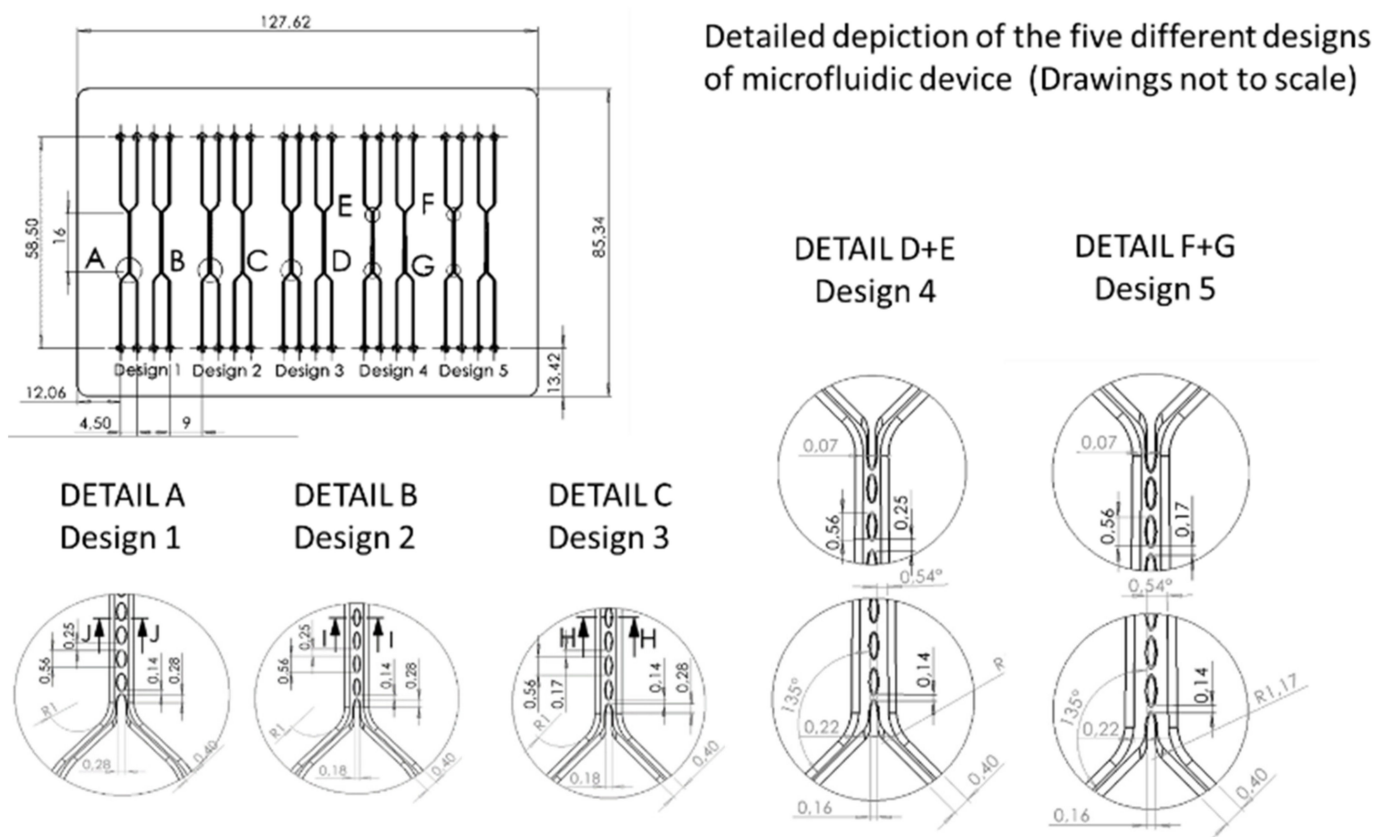


**Figure A1.** Layout of channels and culture areas on the MFC, 5 groups of culture areas with various pillar sizes, designs and spacings were designed (Table A1). The channel depth is 170  $\mu\text{m}$  in all cases.

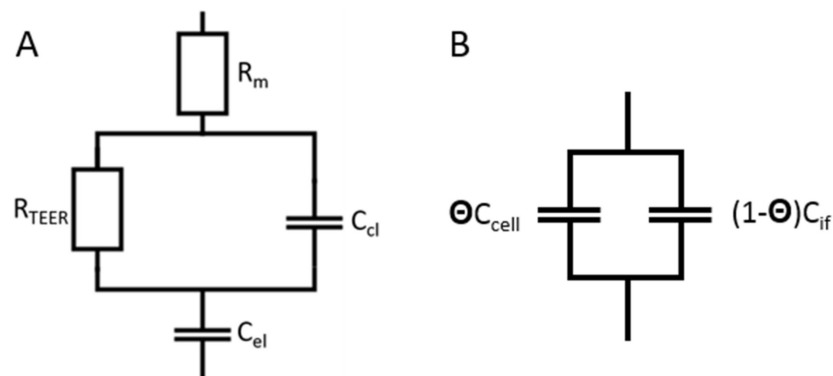


**Figure A2.** (A) Equivalent circuit diagrams employed for impedance spectroscopy data evaluation. (B)  $C_{cl}$  composed of a parallel connection of the capacitance,  $C_{cell}$ , of the cell layer on covered areas and the capacitance of the gel/medium interface,  $C_{if}$ , on areas bare of cells.

TEER was measured by using impedance spectroscopy. The in-house developed system used here generates and applies a discrete spectrum of sinusoidal signals simultaneously to all culture areas on the chip in a parallel fashion. Both voltage and current traces are recorded at a high temporal resolution. Following data acquisition, Fourier transforms of both voltage and current signals are computed and render the impedance spectra, which allow for the determination of several electrical parameters of the system by application of a non-linear fitting algorithm.

The culture area is comprised of the cellular barrier, the gel and medium channel and the electrodes. The electrical properties of this system are reflected by an equivalent circuit according to Figure A2A, including capacitance  $C_{cl}$  and resistance  $R_{TEER}$  of the cellular barrier and the gel/medium interface, respectively, as well as the medium resistance,  $R_m$ , and the electrode capacitance  $C_{el}$ . All parameters can be determined from the spectra by a non-linear fitting algorithm.

The capacitance  $C_{cl}$  can be assumed to be composed of a parallel connection of two capacitors (Figure A2B). Firstly, the capacitance of the cellular layer is determined by the specific capacitance  $C_{cell}$  on the area fraction  $\Theta$ , where the gel is covered by the cell layer. The second capacitor represents the specific capacitance of the gel/medium interface  $C_{if}$  represented by the area fraction  $(1 - \Theta)$  of bare gel/medium interface. Accordingly, the capacitance  $C_{cl}$  determined from the impedance measurement will be given by

$$C_{Cl} = \theta C_{cell} + (1 - \theta)C_{if} \quad (2)$$

from which the coverage of the gel by cells, may be determined as

$$\theta = \frac{(C_{cl} - C_{cell})}{(C_{if} - C_{cell})} \quad (3)$$

with  $C_{cell} \approx 4.5 \times 10^{-6} \text{ F/cm}^2$  and  $C_{if} \approx 2.3 \times 10^{-4} \text{ F/cm}^2$ .

$$R_{TEER} = \frac{R_{TEER}^0 R_{if}^0}{R_{TEER}^0 (1 - \theta) + R_{if}^0 \theta} \quad (4)$$



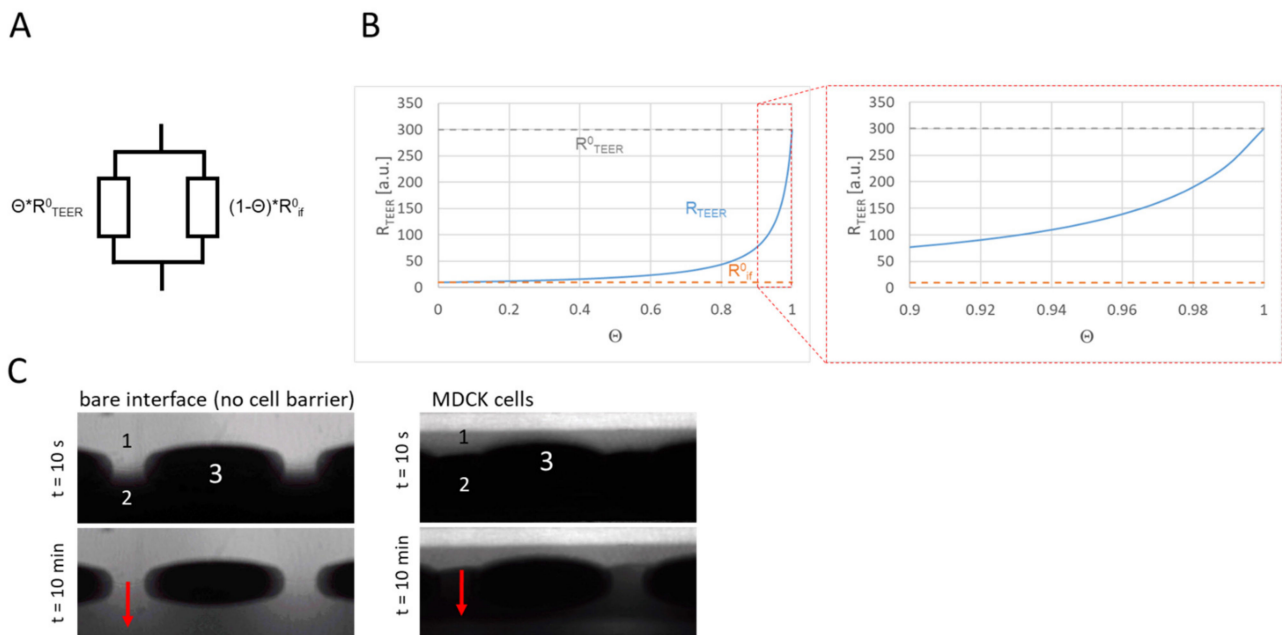


**Figure A3.** Measurement of barrier tightness. (A)  $R_{TEER}$  can be estimated by assuming a parallel connection of the specific resistance,  $R_{TEER}^0$ , on area fractions,  $\Theta$ , of the interface covered by the cell layer and the specific resistance,  $R_{if}^0$ , of the bare interface on the remaining area fraction  $(1 - \Theta)$ , according to (B) Simulation of the resistance,  $R_{TEER}$ , as a function of coverage of the interface. As the resistance of the bare interface,  $R_{if}^0$ , will be much smaller when compared to  $R_{TEER}^0$ , even very small area fractions  $(1 - \Theta)$  uncovered by the cell layer will result in a significant reduction in apparent  $R_{TEER}$  measured by impedance spectroscopy. This simulation demonstrates the sensitivity and usefulness of impedance measurement in assessing the tightness of the cell layer. (C) FITC-dextran (MW = 4 kD) was placed in the perfusion channel and diffusion into the gel phase was monitored by fluorescence video microscopy to assess barrier tightness. 1: perfusion channel, 2: gel phase, 3: pillar. The red arrow indicates the concentration gradient and the direction of diffusion from the perfusion channel into the gel phase. In the absence of a cell layer (left), a significant increase in fluorescence intensity in the gel phase was observed after 10 min, which is indicative of diffusion of the tracer from the perfusion channel into the gel phase, whereas a cell layer comprised of MDCK cells (right) prevented diffusion of the tracer into the gel.

**Table A1.** Dimensions of the MFC chip.

Design	Channel	Pillar Length	Pillar Width	Distance between Pillars	Channel Width	Channel Depth	Chamber Length	Number of Pillars	Combined Area between Pillars
		$\mu\text{m}$	$\mu\text{m}$	$\mu\text{m}$	$\mu\text{m}$	$\mu\text{m}$	mm		$\text{mm}^2$
A	C1	560	160	170	700–1000	170	16	21	0.44
	C2	560	160	170	700–1000	170	16	21	0.44
B	C3	560	160	250	700–1000	170	16	19	0.80
	C4	560	160	250	700–1000	170	16	19	0.80
C	C5	560	180	170	800	170	16	21	0.44
	C6	560	180	170	800	170	16	21	0.44
D	C7	560	180	250	800	170	16	19	0.80
	C8	560	180	250	800	170	16	19	0.80
E	C9	560	280	250	800	170	16	19	0.80
	C10	560	280	250	800	170	16	19	0.80

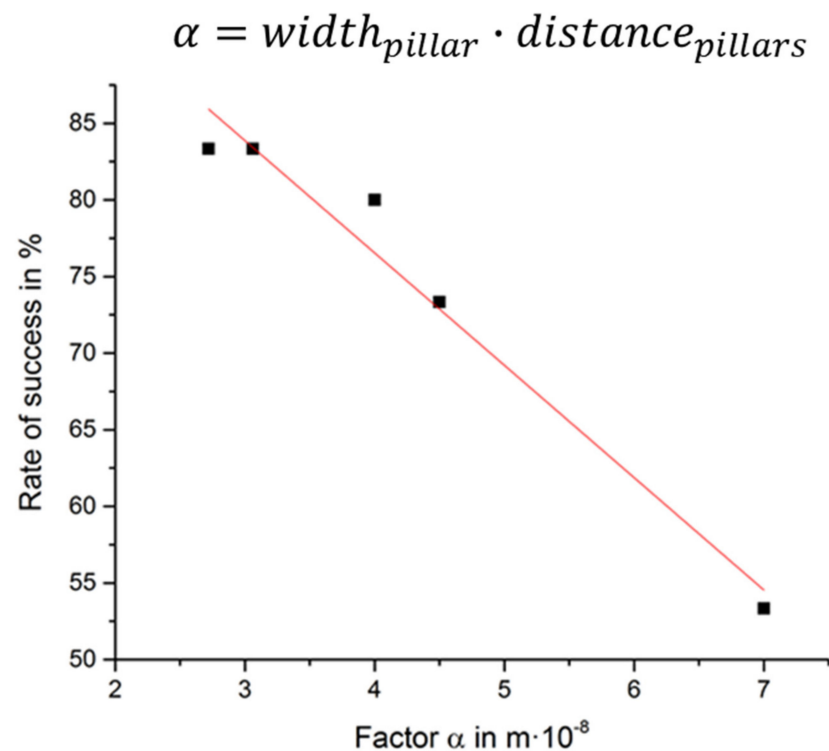


**Figure A4.** Success of priming of MFC with the hydrogel solution depends on pillar size and spacing as reflected by a factor  $\alpha$ , with  $\alpha$  being defined as the product of the pillar width and distance between two adjacent pillars. MFCs were filled at a flow rate of 2.5–3  $\mu\text{L}/\text{min}$  with hydrogel solution. Successful priming is achieved when no spillover occurs and perfusion of the adjacent “luminal” channel remains possible.

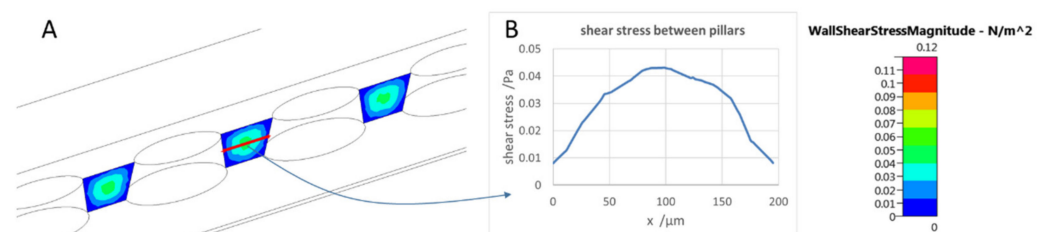


**Figure A5.** (A) Shear stress at the interface between gel phase and perfusion in the MFC determined by multi-physics simulation at a flow rate of 10  $\mu\text{L}/\text{min}$  in the luminal channel. (B) Shear stress varies between 0.01 and 0.045 Pa from the rim to the center of the gap between pillars.

## References

1. Stevens, T.; Garcia, J.G.N.; Shasby, D.M.; Bhattacharya, J.; Malik, A.B. Mechanisms regulating endothelial cell barrier function. *Am. J. Physiol. Cell. Mol. Physiol.* **2000**, *279*, L419–L422. [[CrossRef](#)] [[PubMed](#)]
2. Srinivasan, B.; Kolli, A.R.; Esch, M.B.; Abaci, H.E.; Shuler, M.L.; Hickman, J.J. TEER Measurement techniques for In Vitro barrier model systems. *J. Lab. Autom.* **2015**, *20*, 107–126. [[CrossRef](#)]
3. Weksler, B.B.; Subileau, E.A.; Perrière, N.; Charneau, P.; Holloway, C.J.; Leveque, M.; Tricoire-Leignel, H.; Nicotra, A.; Bourdoulous, S.; Turowski, P.; et al. Blood-brain barrier-specific properties of a human adult brain endothelial cell line. *FASEB J.* **2005**, *19*, 1872–1874. [[CrossRef](#)] [[PubMed](#)]
4. Petty, M.A.; Lo, E.H. Junctional complexes of the blood–brain barrier: Permeability changes in neuroinflammation. *Prog. Neurobiol.* **2002**, *68*, 311–323. [[CrossRef](#)]
5. Bjelobaba, I.; Savic, D.; Lavrnja, I. Multiple sclerosis and neuroinflammation: The overview of current and prospective therapies. *Curr. Pharm. Des.* **2017**, *23*, 693–730. [[CrossRef](#)]
6. Zervantonakis, I.K.; Hughes-Alford, S.K.; Charest, J.L.; Condeelis, J.S.; Gertler, F.B.; Kamm, R.D. Three-dimensional microfluidic model for tumor cell intravasation and endothelial barrier function. *Proc. Natl. Acad. Sci. USA* **2012**, *109*, 13515–13520. [[CrossRef](#)]

7. Heyder, C.; Gloria-Maercker, E.; Entschladen, F.; Hatzmann, W.; Niggemann, B.; Zänker, K.; Dittmar, T. Realtime visualization of tumor cell/endothelial cell interactions during transmigration across the endothelial barrier. *J. Cancer Res. Clin. Oncol.* **2002**, *128*, 533–538.
8. Valastyan, S.; Weinberg, R.A. Tumor metastasis: Molecular insights and evolving paradigms. *Cell* **2011**, *147*, 275–292. [[CrossRef](#)]
9. Weis, S.; Cui, J.; Barnes, L.; Cheresch, D. Endothelial barrier disruption by VEGF-mediated Src activity potentiates tumor cell extravasation and metastasis. *J. Cell Biol.* **2004**, *167*, 223–229. [[CrossRef](#)] [[PubMed](#)]
10. Farhadi, A.; Banan, A.; Fields, J.; Keshavarzian, A. Intestinal barrier: An interface between health and disease. *J. Gastroenterol. Hepatol.* **2003**, *18*, 479–497. [[CrossRef](#)] [[PubMed](#)]
11. Turner, J.R. Intestinal mucosal barrier function in health and disease. *Nat. Rev. Immunol.* **2009**, *9*, 799–809. [[CrossRef](#)]
12. Komarova, Y.; Malik, A.B. Regulation of endothelial permeability via paracellular and transcellular transport pathways. *Annu. Rev. Physiol.* **2010**, *72*, 463–493. [[CrossRef](#)]
13. Alphonsus, C.S.; Rodseth, R. The endothelial glycocalyx: A review of the vascular barrier. *Anaesthesia* **2014**, *69*, 777–784. [[CrossRef](#)]
14. Erdő, F.; Denes, L.; de Lange, E. Age-associated physiological and pathological changes at the blood–brain barrier: A review. *J. Cereb. Blood Flow Metab.* **2017**, *37*, 4–24. [[CrossRef](#)] [[PubMed](#)]
15. Naik, P.; Cucullo, L. In Vitro blood–brain barrier models: Current and perspective technologies. *J. Pharm. Sci.* **2012**, *101*, 1337–1354. [[CrossRef](#)]
16. Sloan, C.D.K.; Nandi, P.; Linz, T.; Aldrich, J.V.; Audus, K.L.; Lunte, S.M. Analytical and biological methods for probing the blood–brain barrier. *Annu. Rev. Anal. Chem.* **2012**, *5*, 505–531. [[CrossRef](#)]
17. Wolff, A.; Antfolk, M.; Brodin, B.; Tenje, M. In Vitro blood–brain barrier models—an overview of established models and new microfluidic approaches. *J. Pharm. Sci.* **2015**, *104*, 2727–2746. [[CrossRef](#)] [[PubMed](#)]
18. Van Der Helm, M.W.; Van Der Meer, A.D.; Eijkel, J.C.; van den Berg, A.; Segerink, L.I. Microfluidic organ-on-chip technology for blood–brain barrier research. *Tissue Barriers* **2016**, *4*, e1142493. [[CrossRef](#)] [[PubMed](#)]
19. Campisi, M.; Shin, Y.; Osaki, T.; Hajal, C.; Chiono, V.; Kamm, R.D. 3D self-organized microvascular model of the human blood–brain barrier with endothelial cells, pericytes and astrocytes. *Biomaterials* **2018**, *180*, 117–129. [[CrossRef](#)] [[PubMed](#)]
20. Yu, F.; Kumar, N.D.S.; Choudhury, D.; Foo, L.C.; Ng, S.H. Microfluidic platforms for modeling biological barriers in the circulatory system. *Drug Discov. Today* **2018**, *23*, 815–829. [[CrossRef](#)]
21. Jiang, L.; Li, S.; Zheng, J.; Li, Y.; Huang, H. Recent progress in microfluidic models of the blood–brain barrier. *Micromachines* **2019**, *10*, 375. [[CrossRef](#)] [[PubMed](#)]
22. Park, T.-E.; Mustafaoglu, N.; Herland, A.; Hasselkus, R.; Mannix, R.; Fitzgerald, E.A.; Prantil-Baun, R.; Watters, A.; Henry, O.; Benz, M.; et al. Hypoxia-enhanced blood–brain barrier chip recapitulates human barrier function and shuttling of drugs and antibodies. *Nat. Commun.* **2019**, *10*, 2621. [[CrossRef](#)] [[PubMed](#)]
23. Lee, C.S.; Leong, K.W. Advances in microphysiological blood–brain barrier (BBB) models towards drug delivery. *Curr. Opin. Biotechnol.* **2020**, *66*, 78–87. [[CrossRef](#)]
24. Hajal, C.; Le Roi, B.; Kamm, R.D.; Maoz, B.M. Biology and models of the blood–brain barrier. *Annu. Rev. Biomed. Eng.* **2021**, *23*, 359–384. [[CrossRef](#)]
25. Pandey, P.K.; Sharma, A.K.; Gupta, U. Blood brain barrier: An overview on strategies in drug delivery, realistic in vitro modeling and in vivo tracking. *Tissue Barriers* **2016**, *4*, e1129476. [[CrossRef](#)] [[PubMed](#)]
26. Zhang, W.; Mehta, A.; Tong, Z.; Esser, L.; Voelcker, N.H. Development of polymeric nanoparticles for blood–brain barrier transfer—strategies and challenges. *Adv. Sci.* **2021**, *8*, 2003937. [[CrossRef](#)]
27. Yeste, J.; Illa, X.; Alvarez, M.; Villa, R. Engineering and monitoring cellular barrier models. *J. Biol. Eng.* **2018**, *12*, 1–19. [[CrossRef](#)]
28. Cucullo, L.; Hossain, M.; Puvenna, V.; Marchi, N.; Janigro, D. The role of shear stress in blood–brain barrier endothelial physiology. *BMC Neurosci.* **2011**, *12*, 40. [[CrossRef](#)]
29. Meigs, L.; Smirnova, L.; Rovida, C.; Leist, M.; Hartung, T. Animal testing and its alternatives—the most important omics is economics. *ALTEX* **2018**, *35*, 275–305. [[CrossRef](#)]
30. Ingber, D.E. Is it time for reviewer 3 to request human organ chip experiments instead of animal validation studies? *Adv. Sci.* **2020**, *7*, 2002030. [[CrossRef](#)]
31. Pound, P.; Ritskes-Hoitinga, M. Is it possible to overcome issues of external validity in preclinical animal research? Why most animal models are bound to fail. *J. Transl. Med.* **2018**, *16*, 304. [[CrossRef](#)] [[PubMed](#)]
32. Low, L.A.; Mummery, C.; Berridge, B.R.; Austin, C.P.; Tagle, D.A. Organs-on-chips: Into the next decade. *Nat. Rev. Drug Discov.* **2021**, *20*, 345–361. [[CrossRef](#)] [[PubMed](#)]
33. Bhalerao, A.; Sivandzade, F.; Archie, S.R.; Chowdhury, E.A.; Noorani, B.; Cucullo, L. In Vitro modeling of the neurovascular unit: Advances in the field. *Fluids Barriers CNS* **2020**, *17*, 22. [[CrossRef](#)]
34. Hachey, S.J.; Hughes, C.C.W. Applications of tumor chip technology. *Lab Chip* **2018**, *18*, 2893–2912. [[CrossRef](#)]
35. Baker, M. Tissue models: A living system on a chip. *Nature* **2011**, *471*, 661. [[CrossRef](#)]
36. Ingber, D.E. Reverse engineering human pathophysiology with organs-on-chips. *Cell* **2016**, *164*, 1105–1109. [[CrossRef](#)]
37. Augustine, R.; Aqel, A.H.; Kalva, S.N.; Joshy, K.; Nayeem, A.; Hasan, A. Bioengineered microfluidic blood–brain barrier models in oncology research. *Transl. Oncol.* **2021**, *14*, 101087. [[CrossRef](#)]
38. Oddo, A.; Peng, B.; Tong, Z.; Wei, Y.; Tong, W.Y.; Thissen, H.; Voelcker, N.H. Advances in microfluidic blood–brain barrier (BBB) models. *Trends Biotechnol.* **2019**, *37*, 1295–1314. [[CrossRef](#)]

39. Ma, Y.-H.V.; Middleton, K.; You, L.; Sun, Y. A review of microfluidic approaches for investigating cancer extravasation during metastasis. *Microsyst. Nanoeng.* **2018**, *4*, 17104. [[CrossRef](#)]
40. Sun, W.; Luo, Z.; Lee, J.; Kim, H.-J.; Lee, K.; Tebon, P.; Feng, Y.; Dokmeci, M.R.; Sengupta, S.; Khademhosseini, A. Organ-on-a-chip for cancer and immune organs modeling. *Adv. Health Mater.* **2019**, *8*, e1801363. [[CrossRef](#)]
41. Toepke, M.W.; Beebe, D.J. PDMS absorption of small molecules and consequences in microfluidic applications. *Lab Chip* **2006**, *6*, 1484–1486. [[CrossRef](#)]
42. Van Meer, B.; de Vries, H.; Firth, K.; Van Weerd, J.; Tertoolen, L.; Karperien, H.; Jonkheijm, P.; Denning, C.; Ijzerman, A.; Mummery, C. Small molecule absorption by PDMS in the context of drug response bioassays. *Biochem. Biophys. Res. Commun.* **2017**, *482*, 323–328. [[CrossRef](#)] [[PubMed](#)]
43. Van Midwoud, P.M.; Janse, A.; Merema, M.T.; Groothuis, G.M.; Verpoorte, E. Comparison of biocompatibility and adsorption properties of different plastics for advanced microfluidic cell and tissue culture models. *Anal. Chem.* **2012**, *84*, 3938–3944. [[CrossRef](#)] [[PubMed](#)]
44. Jena, R.K.; Yue, C.Y. Cyclic olefin copolymer based microfluidic devices for biochip applications: Ultraviolet surface grafting using 2-methacryloyloxyethyl phosphorylcholine. *Biomicrofluidics* **2012**, *6*, 12822–1282212. [[CrossRef](#)] [[PubMed](#)]
45. Schütte, J.; Freudigmann, C.; Benz, K.; Böttger, J.; Gebhardt, R.; Stelzle, M. A method for patterned in situ biofunctionalization in injection-molded microfluidic devices. *Lab Chip* **2010**, *10*, 2551–2558. [[CrossRef](#)]
46. Benson, K.; Cramer, S.; Galla, H.-J. Impedance-based cell monitoring: Barrier properties and beyond. *Fluids Barriers CNS* **2013**, *10*, 5. [[CrossRef](#)]
47. Maier, J.; Traenkle, B.; Rothbauer, U. Real-time analysis of epithelial-mesenchymal transition using fluorescent single-domain antibodies. *Sci. Rep.* **2015**, *5*, 13402. [[CrossRef](#)]
48. Wong, A.D.; Ye, M.; Levy, A.F.; Rothstein, J.D.; Bergles, D.E.; Searson, P.C. The blood-brain barrier: An engineering perspective. *Front. Neuroeng.* **2013**, *6*, 7. [[CrossRef](#)]
49. Desai, S.Y.; Marroni, M.; Cucullo, L.; Krizanac-Bengez, L.; Mayberg, M.R.; Hossain, M.T.; Grant, G.G.; Janigro, D. Mechanisms of Endothelial Survival Under Shear Stress. *Endothelium* **2002**, *9*, 89–102. [[CrossRef](#)]
50. Hagemeyer, B.; Zechnall, F.; Stelzle, M. Towards plug and play filling of microfluidic devices by utilizing networks of capillary stop valves. *Biomicrofluidics* **2014**, *8*, 056501. [[CrossRef](#)]
51. Gijzen, L.; Marescotti, D.; Raineri, E.; Nicolas, A.; Lanz, H.L.; Guerrero, D.; Van Vught, R.; Joore, J.; Vulto, P.; Peitsch, M.C.; et al. An intestine-on-a-chip model of plug-and-play modularity to study inflammatory processes. *SLAS Technol. Transl. Life Sci. Innov.* **2020**, *25*, 585–597. [[CrossRef](#)] [[PubMed](#)]
52. Adriani, G.; Ma, D.; Pavesi, A.; Kamm, R.D.; Goh, E.L.K. A 3D neurovascular microfluidic model consisting of neurons, astrocytes and cerebral endothelial cells as a blood–brain barrier. *Lab Chip* **2016**, *17*, 448–459. [[CrossRef](#)] [[PubMed](#)]
53. Irvine, J.D.; Takahashi, L.; Lockhart, K.; Cheong, J.; Tolan, J.W.; Selick, H.; Grove, J. MDCK (Madin-Darby canine kidney) cells: A tool for membrane permeability screening. *J. Pharm. Sci.* **1999**, *88*, 28–33. [[CrossRef](#)] [[PubMed](#)]
54. Ferrell, N.; Desai, R.R.; Fleischman, A.J.; Roy, S.; Humes, H.D.; Fissell, W.H. A Microfluidic bioreactor with integrated transepithelial electrical resistance (TEER) measurement electrodes for evaluation of renal epithelial cells. *Biotechnol. Bioeng.* **2010**, *107*, 707–716. [[CrossRef](#)] [[PubMed](#)]
55. Chen, Z.-Z.; Lu, Y.; Du, S.-Y.; Shang, K.-X.; Cai, C.-B. Influence of borneol and muscone on geniposide transport through MDCK and MDCK-MDR1 cells as blood–brain barrier in vitro model. *Int. J. Pharm.* **2013**, *456*, 73–79. [[CrossRef](#)] [[PubMed](#)]
56. Esch, M.B.; Ueno, H.; Applegate, D.R.; Shuler, M.L. Modular, pumpless body-on-a-chip platform for the co-culture of GI tract epithelium and 3D primary liver tissue. *Lab Chip* **2016**, *16*, 2719–2729. [[CrossRef](#)] [[PubMed](#)]
57. Henry, O.Y.F.; Villenave, R.; Cronce, M.J.; Leineweber, W.D.; Benz, M.A.; Ingber, D.E. Organs-on-chips with integrated electrodes for trans-epithelial electrical resistance (TEER) measurements of human epithelial barrier function. *Lab Chip* **2017**, *17*, 2264–2271. [[CrossRef](#)]
58. Odijk, M.; Van Der Meer, A.D.; Levner, D.; Kim, H.J.; Van Der Helm, M.W.; Segerink, L.I.; Frimat, J.-P.; Hamilton, G.A.; Ingber, D.E.; Berg, A.V.D. Measuring direct current trans-epithelial electrical resistance in organ-on-a-chip microsystems. *Lab Chip* **2014**, *15*, 745–752. [[CrossRef](#)]
59. Sung, J.H.; Wang, Y.; Shuler, M.L. Strategies for using mathematical modeling approaches to design and interpret multi-organ microphysiological systems (MPS). *APL Bioeng.* **2019**, *3*, 021501. [[CrossRef](#)]